Structural Mechanics Predictions Relating to Clinical Coronary Stent Fracture in a 5 Year Period in FDA MAUDE Database

Citation: Everett, Kay D., Claire Conway, Gerard J. Desany, Brian L. Baker, Gilwoo Choi, Charles A. Taylor, and Elazer R. Edelman. "Structural Mechanics Predictions Relating to Clinical Coronary Stent Fracture in a 5 Year Period in FDA MAUDE Database." Ann Biomed Eng 44, no. 2 (October 14, 2015): 391–403.

As Published: http://dx.doi.org/10.1007/s10439-015-1476-3

Publisher: Springer US

Persistent URL: http://hdl.handle.net/1721.1/103368

Version: Author's final manuscript: final author's manuscript post peer review, without publisher's formatting or copy editing

Author affiliations

Kay D. Everett
Institute for Medical Engineering and Science, MIT, Cambridge, MA, USA
kfurman@mit.edu

Claire Conway
Institute for Medical Engineering and Science, MIT, Cambridge, MA, USA
cconway@mit.edu

Gerard J. Desany
Winchester Engineering and Analytical Center, US Food and Drug Administration, Winchester, MA, USA
Gerard.Desany@fda.hhs.gov

Brian L. Baker
Winchester Engineering and Analytical Center, US Food and Drug Administration, Winchester, MA, USA
Brian.Baker@fda.hhs.gov

Gilwoo Choi
Department of Bioengineering, Stanford University, Stanford, CA, USA
giroo@heartflow.com

Charles A. Taylor
Department of Bioengineering, Stanford University, Stanford, CA, USA
taylor@heartflow.com

Elazer Edelman
Institute for Medical Engineering and Science, MIT, Cambridge, MA, USA
Cardiovascular Division, Brigham and Women’s Hospital, Harvard Medical School, Boston, MA, USA
ere@mit.edu

Structural mechanics predictions relating to clinical coronary stent fracture in a 5 year period in FDA MAUDE database

Abstract

Endovascular stents are the mainstay of interventional cardiovascular medicine. Technological advances have reduced biological and clinical complications but not mechanical failure. Stent strut fracture is increasingly recognized as of paramount clinical importance. Though consensus reigns that fractures can result from material fatigue, how fracture is induced and the mechanisms underlying its clinical sequelae remain ill-defined. In this study, strut fractures were identified in the prospectively maintained Food and Drug Administration's (FDA) Manufacturer and User Facility Device Experience Database (MAUDE), covering years 2006-2011, and differentiated based on specific coronary artery implantation site and device configuration.

These data, and knowledge of the extent of dynamic arterial deformations obtained from patient CT images and published data, were used to define boundary conditions for 3D finite element models incorporating multimodal, multi-cycle deformation. The structural response for a range of stent designs and configurations was predicted by computational models and included estimation of maximum principal, minimum principal and equivalent plastic strains. Fatigue assessment was performed with Goodman diagrams and safe/unsafe regions defined for different stent designs. Von Mises stress and maximum principal strain increased with multimodal, fully reversed deformation. Spatial maps of unsafe locations corresponded to the identified locations of fracture in different coronary arteries in the clinical database.

These findings, for the first time, provide insight into a potential link between patient adverse events and computational modelling of stent deformation. Understanding of the mechanical forces imposed under different implantation conditions may assist in rational design and optimal placement of these devices.

Key words: stent fracture, arterial deformation, finite element analysis

Introduction

Stents now account for greater than 95% of all endovascular interventions. Advances in materials science, pharmacology and controlled drug delivery have nearly eliminated stent restenosis from tissue hyperplasia. Yet, while biological and pathological complications are reduced there remains mechanical device failure, especially strut fracture. With the loss of overriding tissue from the reduction in intimal hyperplasia offered by controlled drug delivery, exposed and penetrating struts take on ever more important impact on the biological response to these implants. Stent strut fracture is an increasingly recognized phenomenon, with rates ranging from 2.6%, for severe, transectional disruption on angiography [1], to 29% when all types of fracture are included at autopsy [2,3]. Clinical investigations have demonstrated that fracture rates rise with stent and lesion length [2–6], multiple, overlapping stents [2,5–9], sirolimus release [10], calcified complex lesions [7,11], relative vessel angulation and "hinge" motion [3,4], higher balloon inflation pressures [12,13], and right coronary artery (RCA) implantation [1,10], in particular in the ostium [4]. When fracture occurs it is associated with higher rates of in-stent restenosis [3,8,10,14,15], thrombosis [2,16,17], and target vessel revascularization [3,4,8,10,15] - outcomes which may be exacerbated by more severe, transectional fractures [2].

Though there is a growing consensus that a proportion of these fractures result from mechanical fatigue [7], what remains ill-defined is how these observational associations lead to increased mechanical stresses and strains as well as the mechanisms underlying fracture initiation of clinical relevance. The stresses and strains encountered in native and stented arteries are poorly understood and are only now being characterized [18–21]. Understanding of all these issues would allow for more precise delineation of rates of fracture, more focused evaluation and assessment of secondary intervention and allow for primary interventions to minimize and reduce the occurrence of clinically significant outcomes associated with stent strut fracture.

The structural performance of stents can be assessed virtually using finite element analysis (FEA). This performance is generally assessed in terms of two major phases: the implantation, short term behavior, and the fatigue response of the device, long term behavior. Considerable attention has been given to implantation behavior and multiple assessments of mechanical characteristics of crimping, deliverability, scaffolding, radial strength, conformability have been reported. The majority of studies focused on deployment and modeling the immediate tissue interactions therein [22–26]. Few have concentrated on why devices fail long after initial implantation, the role of mechanical material fatigue and integrating the highly dynamic *in vivo* environment in which these devices reside. Further, those studies that assess the fatigue response of stents, coronary or peripheral, tend to be limited to consideration of isolated loading modes.

Studies of peripheral stents have focused on long term fatigue response under isolated bending and compression and have largely avoided the clinically observed torsional component. Dordoni *et al.* [27] examined fatigue of a Nitinol superficial femoral arterial (SFA) stent subjected to axial compression and bending with varied stenosis geometries - each cyclic loading mode was examined separately. The FEA results were compared with the Nitinol fatigue strain limit curve, derived from the experimental work of Pelton *et al.* [28]. The predictions did not indicate fatigue failure would occur under the simulated loading conditions, in contrast to clinically observed fracture rates of ~38% in Nitinol SFA stents [5,6]. Early and Kelly [29] also examined the effect of vessel bending and compression, applied separately, on the fatigue life of stainless steel and Nitinol stents. Goodman analysis performed for the former devices plotted the stress amplitude and mean stress for each integration point of the stent elements and indicated a propensity for mechanical failure. In contrast, Nitinol stents were not predicted to fail when a factor of safety was calculated by comparing maximum strain amplitude from FEA with an experimental strain amplitude [28]. Hsiao and Ying [30] used a similar approach where different Nitinol peripheral stent designs under pulsatile pressure loadings were modeled and analyzed with a Goodman analysis, in terms of a fatigue safety factor (FSF). Their computational predictions showed improved FSFs with design alterations but again did not predict fatigue failure. Meoli *et al.* [31] used FEA and Goodman analysis to model previously published *in vitro* fatigue tests of two peripheral stent designs, subjected to either axial compression or bending in air or a constraining tube, and identified relative device performance and predicted fatigue failure at 10^7 cycles, less than a few months of service time at physiological frequencies.

Coronary stents are for the most part stainless steel or chrome alloys and studies of these devices have largely been restricted to analyses of expansion and radial pulsation. Marrey *et al.* [32] used a fracture mechanics based approach to predict the fatigue life of cobalt chromium coronary stents, virtually subjected to a pulsatile radial loading. Though a global stent model post-processed using Goodman analysis did not predict fatigue failure, a local “submodel” of a stent region with postulated flaws analyzed using fracture mechanics techniques defined life of the device in terms of initial flaw size. Li *et al.* [33] reported FEA and experimental results of fatigue tests under pulsatile pressure. While high conformity was achieved between the experimental results and FEA predictions, fatigue failure of the device was not shown. Argente dos Santos *et al*. [34] similarly used a two-scale plasticity damage model with coronary stents virtually subjected to pulsatile pressure loading. Microcracks were predicted to initiate after ~53 to 64 million cycles. Barrera *et al.* [35] presented a fatigue life assessment approach, based on the Dang Van high cycle criterion for coronary stents subjected to cyclic pressure, and even the most critically stressed element did not reach fatigue failure throughout the loading cycle. In a similar study, Azaouzi *et al.* [36] reported fatigue life of pressure loaded coronary stents and post-processed using a Goodman analysis. Fatigue failure was predicted in the extreme case of some 50% expansion of the surrounding idealized artery. Sweeney *et al.* [37,38] used crystal plasticity constitutive theory in a micromechanical fatigue assessment of cobalt chromium stents developing on the work of McGarry *et al.* [39]. 2D and ultimately 3D representative unit cells allowed examination of grain size and orientation on the fatigue life of the device for low cycle [40] and high cycle fatigue [41]. Morlacchi *et al.* [42] investigated the effects of local calcifications on the coronary stent fatigue failure and were the first to include cardiac wall movement which showed that inclusion of cardiac wall movement significantly affected the Goodman analysis results, when compared to pressurization alone. Recently, Auricchio *et al.* [43] presented a computational framework for the lifetime prediction of coronary stents following stent implantation due to pulsation and minor bending angles. The fatigue assessment performed showed that bending significantly reduced predicted lifetime assessment of the device.

All of these works have significantly contributed to our understanding of fatigue behavior of endovascular stents, but they have not explained the high rates of clinically observed fractures, or realistically represented the complex dynamic loading environment in which these devices reside. This work seeks to link the observed complex loading environment with the mechanical state experienced by the stent. The objective is to gain insight into stent fracture through analysis of the arterial locations and device features most often associated with fracture in patients through the use of predictive finite element models of device-level stress and strain under representative multimodal and multi-cycle deformations.

Methods

Prospective Analysis of Stent Strut Fracture Adverse Events in Patients

Adverse event reports of stent fracture were extracted from the FDA MAUDE database over years 2006-2011. The MAUDE database represents prospectively collected reports from clinicians, manufacturers, and patients of adverse events that meet reportability criteria defined as death and serious injury caused or contributed to by a medical device [44]. An initial search of coronary bare metal stent (BMS) and drug eluting stent (DES) records for the terms "strut" and "fracture", followed by manual sorting to remove duplicates and inappropriate results returned 28 BMS and 481 DES reports as valid incidences of stent strut fracture (Table 1). Each report was subsequently analyzed for device and procedural information, which may or may not have been included in the text of the adverse event report (e.g. information was excluded or provided in attached article), including: patient age, implantation duration, target lesion, lesion dimensions, brand name, stent diameter and length, number stents implanted, number fractures, fracture location(s) and severity, and presence and length of overlap. Reports were compared against sex-matched controls selected from adverse event reports from 2006-2011 that were excluded as cases of strut fracture.

Image Acquisition and Deformation Analysis

Cardiac-gated coronary arterial trees were imaged with 64-slice computed tomography (CT) (LightSpeed® VCT 64, GE Healthcare, WI, USA) in seven anonymized patients with prior stent placement, and two patients with native arteries. Patients were retrospectively selected from existing case library and data sets with artifacts at the stented segment that precluded full imaging were excluded from this study. In some patients with stents, in-stent restenosis was observed with calcifications at the stent edges. The average spatial resolution was 0.395 x 0.395 x 0.625 mm3 (matrix size: 512x512x177). Diastole and systole were visually selected by evaluation of ventricular volumes from nine cardiac frames. Vessel shortening (compression), bending, and torsion were extracted in native vessels. Bending deformation was measured by computing the change in curvature of each coronary section over the cardiac cycle. The curvature was measured by computing a best-fit torus to the surface model of the coronary artery [45]. Briefly, a centerline path was first constructed by collecting centroids of cross-sectional lumen along an initial geodesic path on the surface model based on the constraints of minimum cross-sectional area. Then torus parameters (center, radius of torus plane, radius of torus ring, normal vector of torus plane) were optimally computed by minimizing the standard deviation of distances from the surface mesh to the centerline of the torus. For initial values of optimization, the radius and normal plane of the circumscribed circle over the stented region were utilized [18].

Finite Element Models and Goodman Fatigue Analysis

A full description of the finite element and Goodman Fatigue analysis is provided in Supplementary Information. Briefly, 3D stent geometries for delta wing, corrugated ring and multilink designs were created in straight deployed states as well as increasingly long stents, overlapped and stent-in-stent configurations utilizing the delta wing design. The stent material was modeled as solid, homogeneous, elastoplastic 316L stainless steel with strain hardening and dimension-dependent plastic strain.

Deformations were acquired from cardiac-gated CT images described above and supplemented with published strain data for stented coronary [18–21], mid LAD and ostial RCA segments [48] (Table 2). Boundary conditions were applied using multipoint constraints (MPCs), using rigid beam elements as per the approach of [47] and as illustrated in Figure 1 for the delta wing design. Deflections representative of a generic artery case, ostial right (oRCA) and mid-proximal (mpLAD) coronary arteries were chosen.

Following FEA, a Goodman fatigue analysis was performed extracting the maximum principal stresses in the maximally loaded and unloaded states. The mean and alternating stress were calculated, plotted for each of the three stent designs and compared against a critical failure line defined by the fatigue strength and ultimate tensile strength.

Results are presented in terms of contour plots from FEA illustrating spatially the von Mises stress distributions and also the ranges of particular strain variables at the final loading state for each case. The temporal development of this stress state is shown in supplementary material for each of the three stent designs. In addition, the Goodman analysis was spatially plotted to demonstrate predicted unsafe areas.

Statistical Methodology

Categorical variables, presented as frequencies and percentages, were compared with Fisher's exact test. Continuous variables, expressed as mean ± standard error, were compared with Student's paired t test with unequal variance. All p values were 2 sided, and $p<0.05$ was considered statistically significant. Minitab software (State College, PA, USA, v16.2.2) was used for the statistical analyses.

Results

Stent Implantation Parameters Associated with Stent Fracture

Amongst demographics (Table 1) only younger age was associated with fracture (61.4 vs. 66.7 years, p<0.001), suggesting a role for physical activity and cardiac cycling in development of stent fracture. In concert with previous reports [2,52], DES fractures more often involved Cypher stents (Cordis ™, Johnson & Johnson, NJ, USA), though the bare metal backbone Bx Velocity stent (Cordis ™, Johnson & Johnson, NJ, USA) had fracture occurrence on par with other BMS designs (Supplementary Table 1). Differences in stent diameter were trivial between the two patient groups (Table 1); however, patients with stent fracture had longer stents. Further, patients with fracture had both more stents implanted *in toto* and multiple stents in the target vessel. Interestingly, many of these cases (69.8%, when multiple stents implanted) represented implantation of stents in overlapping fashion (Figure 2). Several patients had fractures in other configurations such as stent-in-stent and end-to-end stent placement, though these associations did not reach significance in our data set.

The location of fracture along the stent length varied with implantation conditions. For single stents implanted, the majority of fractures occurred at the mid stent (Figure 2). However, in overlapped stents, fracture most often localized to the stent region adjacent to the overlap site. In stent-in-stent geometries, the majority of fractures localized to the mid stent, as in the case of single stent implantation. With stent-in-stent geometries, the total of all fractures adjacent to the overlap region (e.g. proximal and distal overlap) were equivalent to those in the mid stent region, indicating that stent in stent implantation cases may behave as either a single stent case or an overlap case.

Arterial Locations Associated with Stent Fracture

Adverse events and stent fractures were associated with stent implantation in the RCA (Figure 3). Though previous reports associated fractures with the left anterior descending (LAD) position, we found a statistically identical rate of non-fracture complications in the LAD, perhaps representing the frequency of intervention in this artery. At the same time, perhaps reflecting the different bending stresses on the different coronary arteries, the left circumflex (LCX), left main and branch vessels of the LAD and LCX appeared to be less often associated with fracture in this population.

To assess the stress and strain microenvironment, we stratified the location of implantation along the vessel length (Figure 3). In adverse event reports, patients with fracture were associated with stent implantation in the oRCA, mid proximal LCX and proximal LCX as compared to controls. The association of fractures with oRCA may be indicative of the constrained position at the arterial take off at the base of the heart and focal high curvature evident in this arterial subsegment in some patients, as described below. Interestingly, patients with stents implanted in the distal RCA had fewer reports of adverse events and fracture compared to controls.

Coronary Artery Curvature and Anatomic Variation

Unstented and stented coronary arteries experience significant cyclic shortening, bending, and torsional deflections (Table 2). In general, there is wide variation from one arterial segment to another and from patient to patient. On a per artery basis, stents in the RCA experience significant shortening and bending, in particular. In our analysis, which stratified stent location by vessel subsegment, the smallest radius of curvature (ROC) on EKG-gated CT images, corresponding to the most severe bending angle, was 2.82 cm in the mid proximal RCA, closely followed by the proximal RCA and proximal LAD. Of note, our patient cohort of arterial deflections did not have cases of stent implantation in the oRCA segment. These cases also exhibited an increase in ROC upon systole, perhaps reflecting their relative proximal location (Supplementary Table 2).

Finite Element Models of Arterial Segments Associated with Fracture

Stented arterial segments experience significant dynamic deformation (Table 2) and to our knowledge this is the first time multimodal displacements incorporating combined bending, torsion, and compression have been represented in a finite element model. When uniformly applied boundary conditions, simulating the relatively unconstrained mid LAD segment were applied, the highest von Mises stresses and maximum principal strains were localized to the mid stent region (Figure 4). In contrast, application of a proximal stent constraint with distal displacement resulted in a high ROC as evident in the oRCA position [48] with high von Mises stress and maximum principal strain in the proximal stent segment.

Finite Element Models of Stent Implantation Geometries Associated with Fracture

We evaluated the effect of increasing stent length on the development of stresses and strains when subjected to displacements representative of those observed in stented arterial segments (Figure 5). Increasing stent length resulted in a relatively higher proportion of elements experiencing elevated material strain, as well as strains above that associated with the development of fatigue-type fractures. That longer stents are more prone to fracture, has been reported in the clinical literature. But this is to our knowledge the first report of mechanical evidence for this behavior. Similar to clinical observations, the finite element analyses predicted that for single stents the location of fracture, due to elevated maximum principal strains, localized to the mid stent region and this failure mode was preserved for all stent lengths.

In total, strains developed in overlapped stents exceeded those in single stents. When overall deformation behavior was considered, both overlapped and stent-in-stent geometries predicted focal deformation adjacent to the overlap sites (Figure 5), which complements the clinical observations of fracture location for these implantation conditions. Von Mises stresses exceeding UTS are also noted in the sites adjacent to overlap but as these predictions are in the absence of tissue it is likely that these numbers are overestimates and that the presence of tissue would be associated with less stress in the device.

Finite Element Models of Multimodal Deformation of Stents of Varied Design

Representative symmetric multimodal arterial deformations were applied to stents of varied design, including delta-wing, corrugated ring, and multilink designs, representative of commercially clinically available devices (Figure 6). Interestingly, the multi-cycle deformation behavior and localization of elevated von Mises stress and maximum principal strain were remarkably consistent across stent designs. Examining the strain ranges for each design (Table III) similar ranges are predicted for all three designs in terms of maximum and minimum principal strains. However, high equivalent plastic strain accumulation is predicted for the delta-wing design, consistent with its relatively closed unit cell design. Slight variations in the intra-cyclic deflection behavior, as well as von Mises stress distribution, were observed that were unique to each stent design modeled (Supplementary Videos 1-3).

Goodman Fatigue Analysis

Goodman analysis for the three stent designs subjected to multimodal deformations (Figure 7) confirmed that failure is expected for all three designs in a significant percentage of elements, 10.1% (7074 elements) for the delta-wing, 6.8% (4426 elements) for the corrugated wing and 2.1% (2622 elements) for the open cell design. The spatial locations for the “unsafe” regions (Figure 7) vary with design. The variation of results with each subsequent loading cycle remained stable after 4 loading cycles for the boundary conditions and material model used (Supplementary Figure 1). While the majority of points fall within the “safe” zone of the Goodman diagram, those falling in the “unsafe” zone are of concern, suggesting that, for those boundary conditions examined, high stress and strain are at the level which may result in material failure.

Discussion

Despite increases in adverse event reporting and advances in imaging and monitoring [4,53], the causes and mechanical predictors of stent fracture remain poorly understood. Evaluation and understanding of the clinical phenomenon of stent fracture requires integration of data from adverse events, and finite element models of material fatigue and realistic input parameters and boundary conditions for implanted stent stress and strain. Such integration is understandably challenging and has to date largely been addressed in isolated, single mode analysis, modeling radial pulsation only.

Analysis of patient adverse event reports revealed the artery and device specific pre-implantation conditions associated with the clinical outcome of stent fracture. Importantly, this analysis allows us to deconstruct the specific conditions associated with device dysfunction such that they may be later tested for the true impact of these conditions in representative computational models that probe certain physical conditions of interest. Drug eluting stents represented the majority of adverse events in the MAUDE database reflecting either a preference in use or reporting, or perhaps a different integrated chemical-biological-mechanical phenomenon underlying fracture events in DES. Our results suggest the former, as adverse event reports secondary to fracture had similar DES use to non-fracture events. However, future work should investigate the potential for differential arterial response secondary to strut fracture when drugs are eluted from stents and possible pharmacological, biological and physical interplay in fatigue failure. Clinical fracture reports were also associated with stent length and the use of multiple, overlapping stents (Table 1, Figure 2). The end of stents closest to the coronary ostium may be more prone to fracture compared to the segments farther away (Figure 2), due to the apex-to-base motion of the heart and tethering of the coronary artery by the aorta. Our results further suggest that large stresses and strains result from dynamic changes in curvature, which result in stress and strain concentrations. Load concentration can also explain the predilection for clinical fractures when long and/or multiple stents are used. Long stents will be subject to a greater bending deflection for a given radius of curvature and thus experience higher material strains (Figure 5), and the stent region adjacent to the overlap site in overlapped and stent-in-stent implantation geometries represents a relative discontinuity in longitudinal stiffness that concentrates stress and strain which further localizes fracture to the regions adjacent to overlap.

Specific arterial location and stent geometrical parameters identified in adverse outcomes correlated well with mechanical stress and strain concentrations when recapitulated in finite element models with representative arterial deformations. The RCA, in particular the ostial RCA, mid proximal LCX, and proximal LCX were associated with clinically evident fracture (Figure 3). These regions are especially subjected to high, dynamic changes in curvature. Though the individual geometries and deflections are patient-specific and span a wide range across the physiologic spectrum, it is assumed generalizable to the population at large where such conditions exist. Finite element models showed material stress and strain concentrations along the length of the stent in good agreement with the same regions implicated in clinical reports of fracture (Figure 4). While we did not explicitly model stent fracture initiation or propagation, we do provide evidence for the underlying mechanical force. For the first time finite element predictions showed how multimodal deformations and acute changes in curvature, as evident in the ostial RCA for example, can result in strain concentrations at the proximal stent region. Additionally, when a relatively unconstrained case with multimodal displacement is considered, material stress and strain localizes to the mid stent region. Overlap and stent-in-stent implantation cases revealed similar regions of concern that correlated with those regions implicated in clinical observations of the same.

Finally, the regions of high von Mises stress, maximum and minimum principal strains, and equivalent plastic strain, in delta-wing, corrugated ring, and multilink designs transcend design in part when cyclic deformations were kept constant (Figure 6, Table III, Supplementary Videos 1-3). Each individual design experienced slight differences in magnitude and distribution of material strains, likely due to differences in unit cell, strut thickness, and number of connectors and links along the radial and longitudinal directions but overall patterns were similar. Thus, though there are unique features evident in each arterial and device specific system, these differences can be realistically modeled using advanced computational methods. Further, stress and strain concentration predictions can be used to assess for potentially unsafe regions such as in the Goodman analysis (Figure 7), which indicated a significant percentage of elements fall within the "unsafe" region for all three designs. These results highlight the need for consideration of multimodal deformations in assessing stent performance and for design of next generation devices.

Clinical observational studies have assessed the clinical associations of stent fracture [1,4,6], but these have largely been separate from mechanistic computational studies and previous reports cannot comment on how severity or nature of fracture might contribute to extent of clinical consequence. Our findings support the findings of previous reports but also extend and most importantly begin to explain them. In this way we can now direct attention to clinically meaningful and mechanistically robust analysis of specific fracture modalities and areas of the arterial tree to more closely scrutinize or more precisely rule out strut fracture as a potential contribution or complication in specific patient subsets or clinical scenarios. Thus, with a more inclusive perspective of the range of clinical fractures, we can begin to tease out the spectrum of clinical consequences and variability therein based not only on the type of fracture evident but the potential for more severe fractures to propagate thereafter.

Also to be acknowledged are the limitations of this work. The FDA MAUDE database is a user-initiated, prospectively maintained reporting system that though may not represent the full burden of clinical cases, given the significant incidence of stent fracture reported it was deemed indicative of the problem and analyzed here. The applied boundary conditions were derived from a finite number of patients - a larger data set may provide slight differences in numerical values. Also, because these values represent a spectrum of patients, and were not all collected from similar locations along the length of the artery, we did not seek to replicate any exact set of these conditions. Rather, we chose representative values for compression, bending, and torsion that were within the range of what might be expected in a dynamically strained coronary artery.

Yet, this study does demonstrate the effect of representative deformations, which admittedly may vary slightly per design, as a first step towards a more thorough examination of device performance. Though the arterial segment cases presented rely on representative boundary conditions and our understanding of coronary dynamics, they provide an interesting first look at the potential deformation mechanisms that may underlie the elevated stresses and strains in the regions associated with fracture in patients. Thus, the current analysis is limited to a representative set boundary conditions that does not attempt to fully characterize what indeed are a wide array of possible *in vivo* deformations. Additionally, finite element stent materials were represented as biomedical grade stainless steel 316L but other alloys could have been modeled such as cobalt chromium. The selection of 316L was deemed acceptable for comparison purposes. The effects of crimping and deployment were not included in the finite element models and ongoing work is examining the combined effects of deployment and subsequent multimodal loading. Additionally, though contact between stent elements in a single stent were considered, contact between overlapping stents was not. None-the-less, this study shows the significant effect that multimodal loading has on device performance and this is the first time such an approach has been taken. The finite element models presented predict multimodal stent deformations without an artery present. The effect of stent oversizing and arterial pathology is therefore not assessed. We expect that these components will likely add to the material stress and strain states predicted, though additional work is needed. As the use of MPCs necessarily introduce point discontinuities in applied and observed deformations, addition of a surrounding vessel would also allow for application of a non-uniform deformation gradient along the length of the stent, as in reality the whole stent body will be subject to non-uniform loading and this will have an impact on the stresses generated.

Also to be acknowledged are the limitations of the Goodman approach due to its base formulation, it is derived from the overall macroscale behavior of engineering components and applied here at the scale of individual finite elements. Finally, though our work represents a first step toward more complex multimodal modeling, future work would benefit from more complex computational modeling of fatigue, fracture, and material evolution which should utilize more microscale-based and physically-based prediction methodologies.

Our results suggest that though there are unique and appreciable differences in arterial deflections and stent design for any given patient and procedure, there are underlying mechanistic concepts driving regional development of device stress and strain that can one day be leveraged to predict the localization of fracture in patients. Our results provide the first associations of stent and artery conditions of interest identified in fracture adverse events in United States' patients with computational mechanical models that can incorporate the multimodal, multi-cycle deformation behavior of multiple stent designs with specific implantation conditions associated with clinically significant stent fracture.

Acknowledgements

This work was funded in part by grants from FDA Office of Regulatory Affairs, R01 GM49039 (ERE) from the National Institute of Health, and appointment to the Research Participation Program at FDA administered by Oak Ridge Institute for Science and Education (CC).

Disclosures

Drs Choi and Taylor are employees of and have equity interest in HeartFlow, Inc. Other authors report no conflicts.

References

1. Aoki J, Nakazawa G, Tanabe K, Hoye A, Yamamoto H, Nakayama T, et al.: Incidence and clinical impact of coronary stent fracture after sirolimus-eluting stent implantation. Catheter Cardiovasc Interv 2007 Feb 15;69:380–386.

2. Nakazawa G, Finn AV, Vorpahl M, Ladich E, Kutys R, Balazs I, et al.: Incidence and Predictors of Drug-Eluting Stent Fracture in Human Coronary ArteryA Pathologic Analysis. J Am Coll Cardiol 2009 Nov 17;54:1924–1931.

3. Ino Y, Toyoda Y, Tanaka A, Ishii S, Kusuyama Y, Kubo T, et al.: Predictors and Prognosis of Stent Fracture After Sirolimus-Eluting Stent Implantation. Circ J 2009;73:2036–2041.

4. Popma JJ, Tiroch K, Almonacid A, Cohen S, Kandzari DE, Leon MB: A Qualitative and Quantitative Angiographic Analysis of Stent Fracture Late Following Sirolimus-Eluting Stent Implantation. Am J Cardiol 2009 Apr 1;103:923–929.

5. Iida O, Nanto S, Uematsu M, Morozumi T, Kotani J, Awata M, et al.: Effect of exercise on frequency of stent fracture in the superficial femoral artery. Am J Cardiol 2006 Jul 15;98:272–274.

6. Scheinert D, Scheinert S, Sax J, Piorkowski C, Bräunlich S, Ulrich M, et al.: Prevalence and clinical impact of stent fractures after femoropopliteal stenting. J Am Coll Cardiol 2005 Jan 18;45:312–315.

7. Halwani DO, Anderson PG, Brott BC, Anayiotos AS, Lemons JE: The role of vascular calcification in inducing fatigue and fracture of coronary stents. J Biomed Mater Res B Appl Biomater 2012 Jan 1;100B:292–304.

8. Chung W-S, Park C-S, Seung K-B, Kim P-J, Lee J-M, Koo B-K, et al.: The incidence and clinical impact of stent strut fractures developed after drug-eluting stent implantation. Int J Cardiol 2008 Apr 25;125:325–331.

9. Duda SH, Pusich B, Richter G, Landwehr P, Oliva VL, Tielbeek A, et al.: Sirolimus-Eluting Stents for the Treatment of Obstructive Superficial Femoral Artery Disease Six-Month Results. Circulation 2002 Sep 17;106:1505–1509.

10. Park KW, Park JJ, Chae I-H, Seo J-B, Yang H-M, Lee H-Y, et al.: Clinical characteristics of coronary drug-eluting stent fracture: insights from a two-center des registry. J Korean Med Sci 2011 Jan;26:53–58.

11. Ling AJ, Mwipatayi P, Gandhi T, Sieunarine K: Stenting for carotid artery stenosis: Fractures, proposed etiology and the need for surveillance. J Vasc Surg 2008 Jun 1;47:1220–1226.

12. Min P-K, Yoon Y-W, Moon Kwon H: Delayed strut fracture of sirolimus-eluting stent: a significant problem or an occasional observation? Int J Cardiol 2006 Jan 26;106:404–406.

13. Sianos G, Hofma S, Ligthart JMR, Saia F, Hoye A, Lemos PA, et al.: Stent fracture and restenosis in the drug-eluting stent era. Catheter Cardiovasc Interv 2004 Jan 1;61:111–116.

14. Serikawa T, Kawasaki T, Koga H, Orita Y, Ikeda S, Goto Y, et al.: Late catch-up phenomenon associated with stent fracture after sirolimus-eluting stent implantation: incidence and outcome. J Intervent Cardiol 2011 Apr;24:165–171.

15. Umeda H, Kawai T, Misumida N, Ota T, Hayashi K, Iwase M, et al.: Impact of sirolimus-eluting stent fracture on 4-year clinical outcomes. Circ Cardiovasc Interv 2011 Aug;4:349–354.

16. Park J-S, Shin D-G, Kim Y-J, Hong G-R, Cho I-H: Acute myocardial infarction as a consequence of stent fracture and plaque rupture after sirolimus-eluting stent implantation. Int J Cardiol 2009 May 15;134:e79–81.

17. Choe H, Hur G, Doh JH, Namgung J, Lee SY, Park KT, et al.: A case of very late stent thrombosis facilitated by drug eluting stent fracture: comparative images before and after stent fracture detected by 64-multidetector computed tomography. Int J Cardiol 2009 Apr 17;133:e125–128.

18. Choi G, Cheng CP, Wilson NM, Taylor CA: Methods for quantifying three-dimensional deformation of arteries due to pulsatile and nonpulsatile forces: implications for the design of stents and stent grafts. Ann Biomed Eng 2009 Jan;37:14–33.

19. Ding Z, Zhu H, Friedman MH: Coronary Artery Dynamics In Vivo. Ann Biomed Eng 2002 Apr 1;30:419–429.

20. Liao R, Chen S-YJ, Messenger JC, Groves BM, Burchenal J e. b., Carroll JD: Four-dimensional analysis of cyclic changes in coronary artery shape. Catheter Cardiovasc Interv 2002 Mar 1;55:344–354.

21. Zhu H, Warner JJ, Gehrig TR, Friedman MH: Comparison of coronary artery dynamics pre- and post-stenting. J Biomech 2003 May;36:689–697.

22. Early M, Lally C, Prendergast PJ, Kelly DJ: Stresses in peripheral arteries following stent placement: a finite element analysis. Comput Methods Biomech Biomed Engin 2009;12:25–33.

23. Lally C, Dolan F, Prendergast PJ: Cardiovascular stent design and vessel stresses: A finite element analysis. J Biomech 2005;38:1574–1581.

24. LaDisa JF, Olson LE, Douglas HA, Warltier DC, Kersten JR, Pagel PS: Alterations in regional vascular geometry produced by theoretical stent implantation influence distributions of wall shear stress: analysis of a curved coronary artery using 3D computational fluid dynamics modeling. Biomed Eng OnLine 2006 Jun 16;5:40.

25. Conway C, Sharif F, McGarry J, McHugh P: A Computational Test-Bed to Assess Coronary Stent Implantation Mechanics Using a Population-Specific Approach. Cardiovasc Eng Technol 2012;3:1–14.

26. Conway C, McGarry JP, McHugh PE: Modelling of Atherosclerotic Plaque for Use in a Computational Test-Bed for Stent Angioplasty. Ann Biomed Eng 2014 Sep 11;42:2425–2439.

27. Dordoni E, Meoli A, Wu W, Dubini G, Migliavacca F, Pennati G, et al.: Fatigue behaviour of Nitinol peripheral stents: the role of plaque shape studied with computational structural analyses. Med Eng Phys 2014 Jul;36:842–849.

28. Pelton AR, Schroeder V, Mitchell MR, Gong X-Y, Barney M, Robertson SW: Fatigue and durability of Nitinol stents. J Mech Behav Biomed Mater 2008 Apr;1:153–164.

29. Early M, Kelly DJ: The consequences of the mechanical environment of peripheral arteries for nitinol stenting. Med Biol Eng Comput 2011 Nov;49:1279–1288.

30. Hsiao H-M, Yin M-T: An intriguing design concept to enhance the pulsatile fatigue life of self-expanding stents. Biomed Microdevices 2014 Feb;16:133–141.

31. Meoli A, Dordoni E, Petrini L, Migliavacca F, Dubini G, Pennati G: Computational Modelling of In Vitro Set-Ups for Peripheral Self-Expanding Nitinol Stents: The Importance of Stent–Wall Interaction in the Assessment of the Fatigue Resistance. Cardiovasc Eng Technol 2013 Dec 1;4:474–484.

32. Marrey RV, Burgermeister R, Grishaber RB, Ritchie RO: Fatigue and life prediction for cobalt-chromium stents: A fracture mechanics analysis. Biomaterials 2006 Mar;27:1988–2000.

33. Li J, Luo Q, Xie Z, Li Y, Zeng Y: Fatigue life analysis and experimental verification of coronary stent. Heart Vessels 2010 Jul 1;25:333–337.

34. Argente dos Santos HAF, Auricchio F, Conti M: Fatigue life assessment of cardiovascular balloon-expandable stents: A two-scale plasticity–damage model approach. J Mech Behav Biomed Mater 2012 Nov;15:78–92.

35. Barrera O, Makradi A, Abbadi M, Azaouzi M, Belouettar S: On high-cycle fatigue of 316L stents. Comput Methods Biomech Biomed Engin 2014;17:239–250.

36. Azaouzi M, Makradi A, Petit J, Belouettar S, Polit O: On the numerical investigation of cardiovascular balloon-expandable stent using finite element method. Comput Mater Sci 2013 Nov;79:326–335.

37. Sweeney CA, O’Brien B, McHugh PE, Leen SB: Experimental characterisation for micromechanical modelling of CoCr stent fatigue. Biomaterials 2014 Jan;35:36–48.

38. Sweeney CA, McHugh PE, McGarry JP, Leen SB: Micromechanical methodology for fatigue in cardiovascular stents. Int J Fatigue 2012;44:202–216.

39. McGarry JP, O’Donnell BP, McHugh PE, McGarry JG: Analysis of the mechanical performance of a cardiovascular stent design based on micromechanical modelling. Comput Mater Sci 2004;31:421–438.

40. Sweeney CA, O’Brien B, Dunne FPE, McHugh PE, Leen SB: Strain-gradient modelling of grain size effects on fatigue of CoCr alloy. Acta Mater 2014 Oct 1;78:341–353.

41. Sweeney CA, O′Brien B, Dunne FPE, McHugh PE, Leen SB: Micro-scale testing and micromechanical modelling for high cycle fatigue of CoCr stent material. J Mech Behav Biomed Mater 2015 Jun;46:244–260.

42. Morlacchi S, Pennati G, Petrini L, Dubini G, Migliavacca F: Influence of plaque calcifications on coronary stent fracture: A numerical fatigue life analysis including cardiac wall movement. J Biomech 2014 Mar 3;47:899–907.

43. Auricchio F, Constantinescu A, Conti M, Scalet G: A computational approach for the lifetime prediction of cardiovascular balloon-expandable stents. Int J Fatigue 2015 Jun;75:69–79.

44. CFR - Code of Federal Regulations Title 21 [Internet] [cited 2014 Jun 4];Available from: http://www.accessdata.fda.gov/scripts/cdrh/cfdocs/cfcfr/cfrsearch.cfm?fr=803.19

45. Choi G: In vivo quantification of arterial deformation due to pulsatile and non-pulsatile forces: Implications for the design of stents and stent -grafts [Internet] 2009 [cited 2014 Jun 4];Available from: http://gradworks.umi.com/33/82/3382704.html

46. Harewood FJ, McHugh PE: Modeling of Size Dependent Failure in Cardiovascular Stent Struts under Tension and Bending. Ann Biomed Eng 2007;35:1539–1553.

47. Wu W, Yang D-Z, Qi M, Wang W-Q: An FEA method to study flexibility of expanded coronary stents. J Mater Process Technol 2007 Apr 12;184:447–450.

48. Messenger JC, Chen SY, Carroll JD, Burchenal JE, Kioussopoulos K, Groves BM: 3D coronary reconstruction from routine single-plane coronary angiograms: clinical validation and quantitative analysis of the right coronary artery in 100 patients. Int J Card Imaging 2000 Dec;16:413–427.

49. Dang-Van K: Macro-Micro Approach in High-Cycle Multiaxial Fatigue; in McDowell DL, Ellis R (eds): Advances in Multiaxial Fatigue, ASTM International. ASTM International, 1993, pp 120–130.

50. Sines G, Ohgi G: Fatigue Criteria Under Combined Stresses or Strains. J Eng Mater Technol 1981 Apr 1;103:82–90.

51. Crossland B: Effect of large hydrostatic pressures on the torsional fatigue strength of an alloy steel. Proc Int Conf Fatigue Met Inst Mech Eng Lond 1956;138.

52. Park M-W, Chang K, Her SH, Lee J-M, Choi Y-S, Kim D-B, et al.: Incidence and clinical impact of fracture of drug-eluting stents widely used in current clinical practice: comparison with initial platform of sirolimus-eluting stent. J Cardiol 2012 Sep;60:215–221.

53. Jaff M, Dake M, Pompa J, Ansel G, Yoder T: Standardized evaluation and reporting of stent fractures in clinical trials of noncoronary devices. Catheter Cardiovasc Interv 2007 Sep 1;70:460–462.

Table I Baseline Demographic Characteristics and Implantation Conditions Associated with Stent Fracture

Characteristic	Fx + (*n*=509)	Fx - (*n*=506)	p Value
Demographics			
Age, mean ± SE	61.4 ± 0.74	66.7 ± 0.77	<0.001
Women [*n* (%)]	80 (23.7%)	81 (28.8%)	0.17
Stent dimensions, mean ± SE			
Stent diameter, mm	3.0 ± 0.02	2.9 ± 0.02	<0.001
Stent length, mm	24.2 ± 0.36	19.5 ± 0.31	<0.001
Stents implanted, mean ± SE	2.0 ± 0.06	1.1 ± 0.04	<0.001
Stents in vessel [*n* (%)]			
1	255 (50.3%)	331 (67.4%)	<0.001
>1	252 (49.7%)	68 (13.8%)	<0.001
Overlapped stents [*n* (%)]*	176 (69.8%)	11 (16.2%)	<0.001
Stent-in-stent [*n* (%)]*	35 (13.9%)	10 (14.7%)	0.71
Vessels stented, mean ± SE	1.2 ± 0.02	0.9 ± 0.02	<0.001
Target vessel [*n* (%)]			
RCA	263 (52.2%)	125 (28.4%)	<0.001
LAD	150 (29.8%)	143 (32.5%)	0.40
LCX	34 (6.7%)	80 (18.2%)	<0.001
LM	4 (0.8%)	13 (3.0%)	0.01
Diagonal (LAD)	7 (1.4%)	19 (4.3%)	0.008
Marginal (LCX)	8 (1.6%)	24 (5.5%)	0.002
Other	38 (7.5%)	36 (8.2%)	0.72

Values are mean ± SE or n (%). Fx+ = Patients with adverse events and stent fracture, Fx- = Patients with adverse events not including stent fracture. *Overlapped and stent-in-stent values reported as a percentage of those reports where multiple stents were employed.

LAD = left coronary artery, LCX = left circumflex, LM = left marginal, RCA = right coronary artery

Table II Native and Stented Coronary Artery Displacements

	Unstented			Stented		
Parameter	LAD	RCA	Ref.	LAD	RCA	Ref.
Shortening (%)	4.2	2.9	[*]	5.0	7.7	[21]
	6.7	†	[18]			
	8.1	†	[19]			
Bending (°)	7.9	6.8	[*]	10.6	7.1	[*]
	25	25	[20]			
Torsion				†	†	
(°)	7.0	5.7	[*]			
(°)	6.0	†	[18]			
(cm^{-1})	8.6	4.5	[19]			

* = Present study, † = none available

Table III Predicted strain for three uniformly deformed designs. Values represent strain range at the end of each simulation following four fully reversed cycles of simultaneous bending, torsion, and compression.

	PEEQ (%)		Max Principal ε (%)		Min Principal ε (%)	
Design	Max	Min	Max	Min	Max	Min
Delta Wing	307.2	0	48.2	-0.1	0	51.0
Corrugated Wing	95.5	0	49.1	0	0	-97.1
Open Cell	92.7	0	61.5	0	0	-73.1

Reported variables are equivalent plastic strain (PEEQ), maximum principal strain and minimum principal strain.

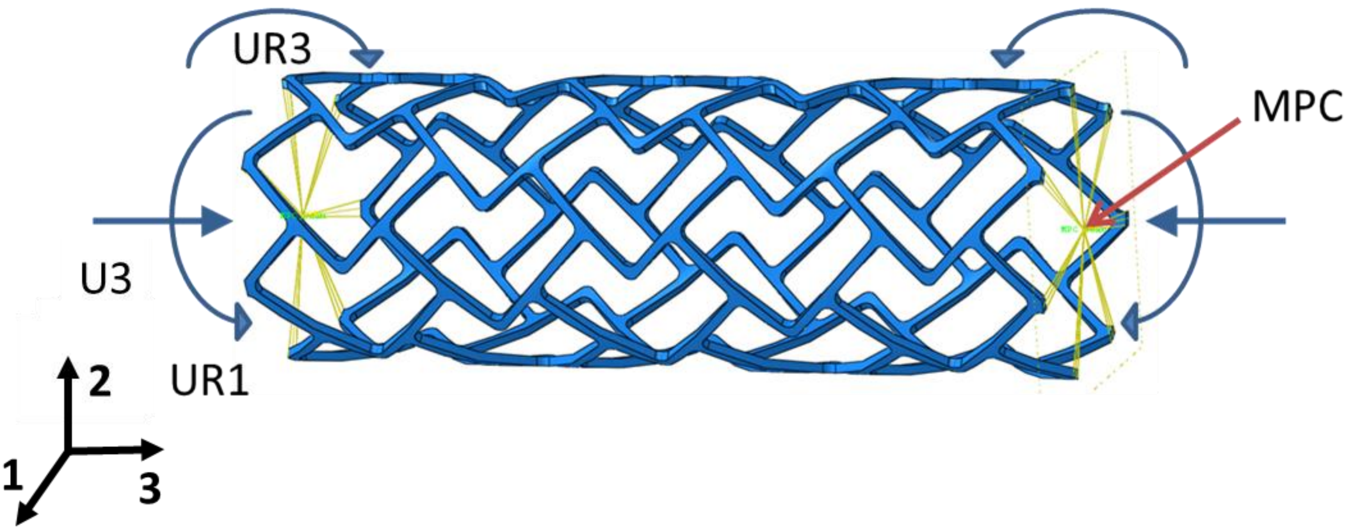

Case	U3	UR1	UR3
Generic	4%, -4%	7°, -7°	3°, -3°
oRCA*	0, -8%	0, -25°	0, -6°
mpLAD*	2.5%, -2.5%	53°, -53°	7°, -7°

Figure 1 Boundary conditions (values displayed denote left, right side of stent - U_n denotes translational deformation and UR_n denotes rotational deformation) and multipoint constraints (MPC) designations. Schematic for the delta wing design (top) and specific deformations and constraints for each case analyzed. Boundary conditions representative of the stented arterial displacements observed in the coronary tree were applied in the generic case of uniform deformation. oRCA and mpLAD conditions were approximated from similar observed displacements in these segments. *Modeled in single (delta wing) design only. Deformations in U2, U3 and rotation in UR2 were fixed in each case.

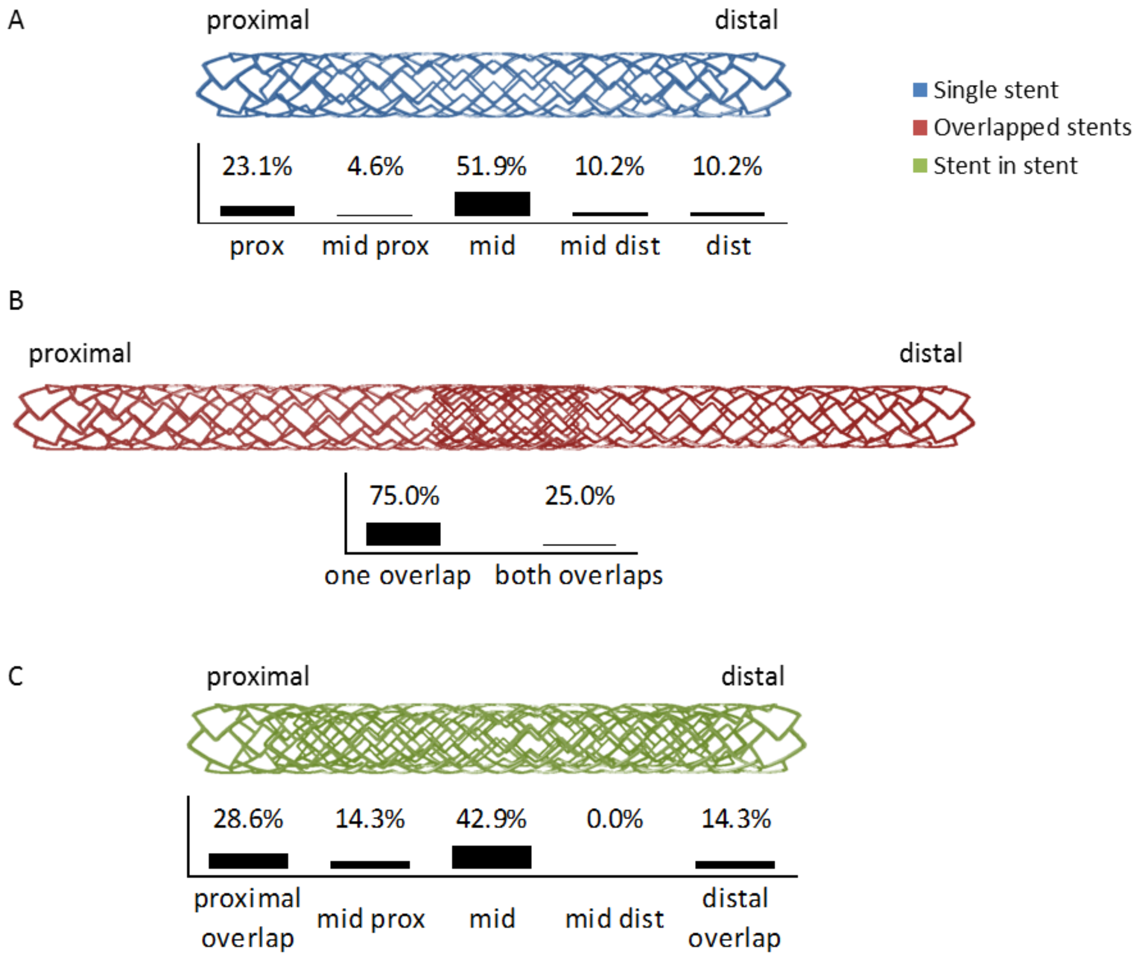

Figure 2 Location of Fracture by Stent Implantation Geometry – While fractures in the 108 individual stents (A) and 9 stent-in-stent (C) reported cases were most prominently located in the midportion, the fractures in the 80 overlap stents occurred principally at the stent region adjacent to the overlap site (s) (B).

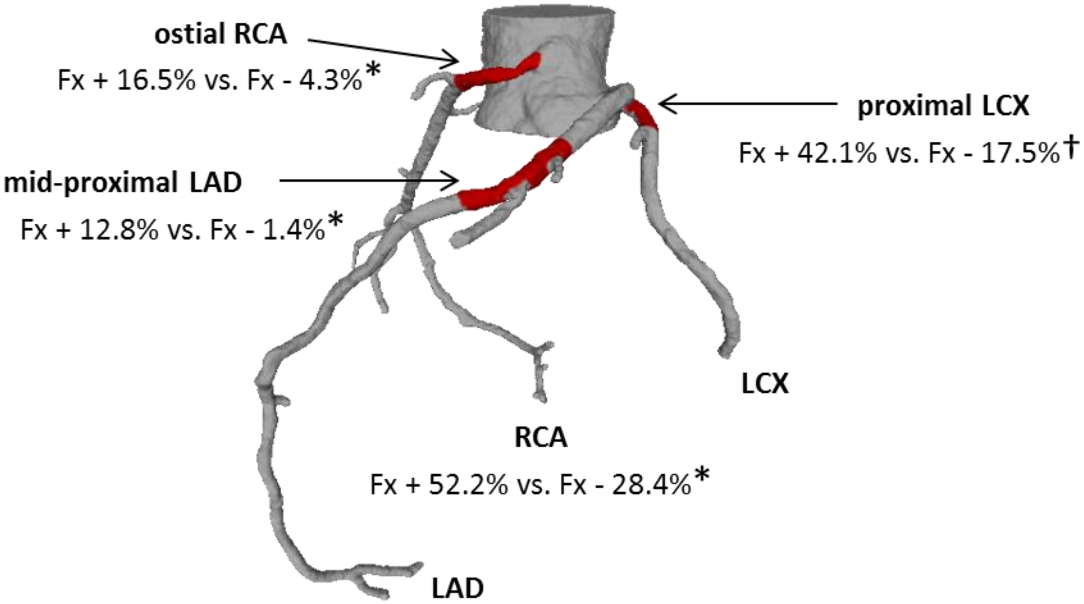

Figure 3 Implantation Sites Associated with Stent Strut Fracture – Stent implantation in patients with fracture and adverse events occurred more often in the ostial RCA, mid-proximal LAD, and proximal LCX. Fx+ = Patients with adverse events and stent fracture, Fx- = patients with adverse events not including stent fracture. *= significant at $p<0.01$, †=significant $p<0.05$.

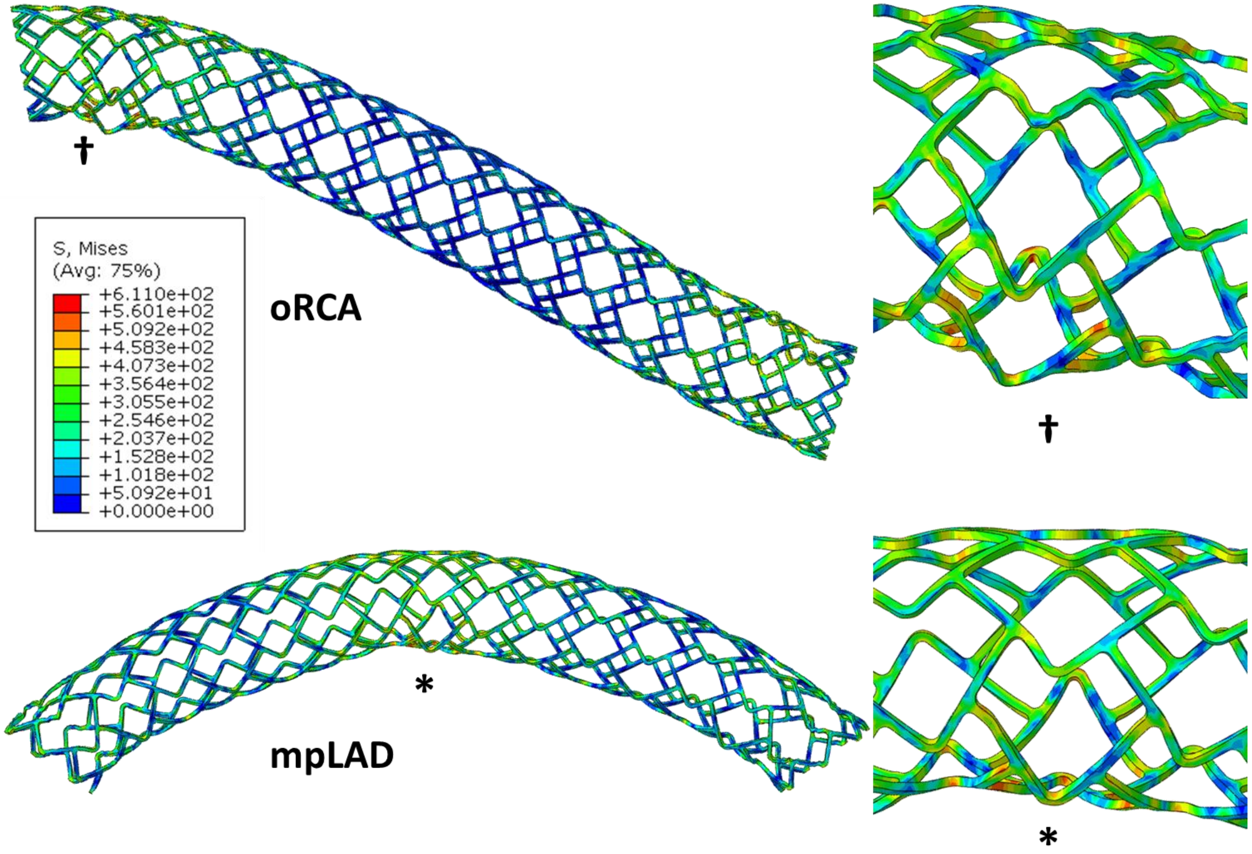

Figure 4 Artery Segment Models of Stent Deformations – Controlled deformations induce stress concentrations in regions that correlate with intra-device fracture location in patients. oRCA (ostial right coronary artery - top) represents a case of unilaterally constrained deformation that leads to severe focal deformation that is clinically suggestive of proximal fractures in the RCA, and mpLAD (mid-proximal left anterior descending - bottom) is the case of uniform end deformations that result in stress concentrations and deformation in the mid stent representative of what is observed in the LAD coronary artery in patients. The symbols denote regions of highest von Mises stress (inset) and match clinical reports of location of stent fracture.

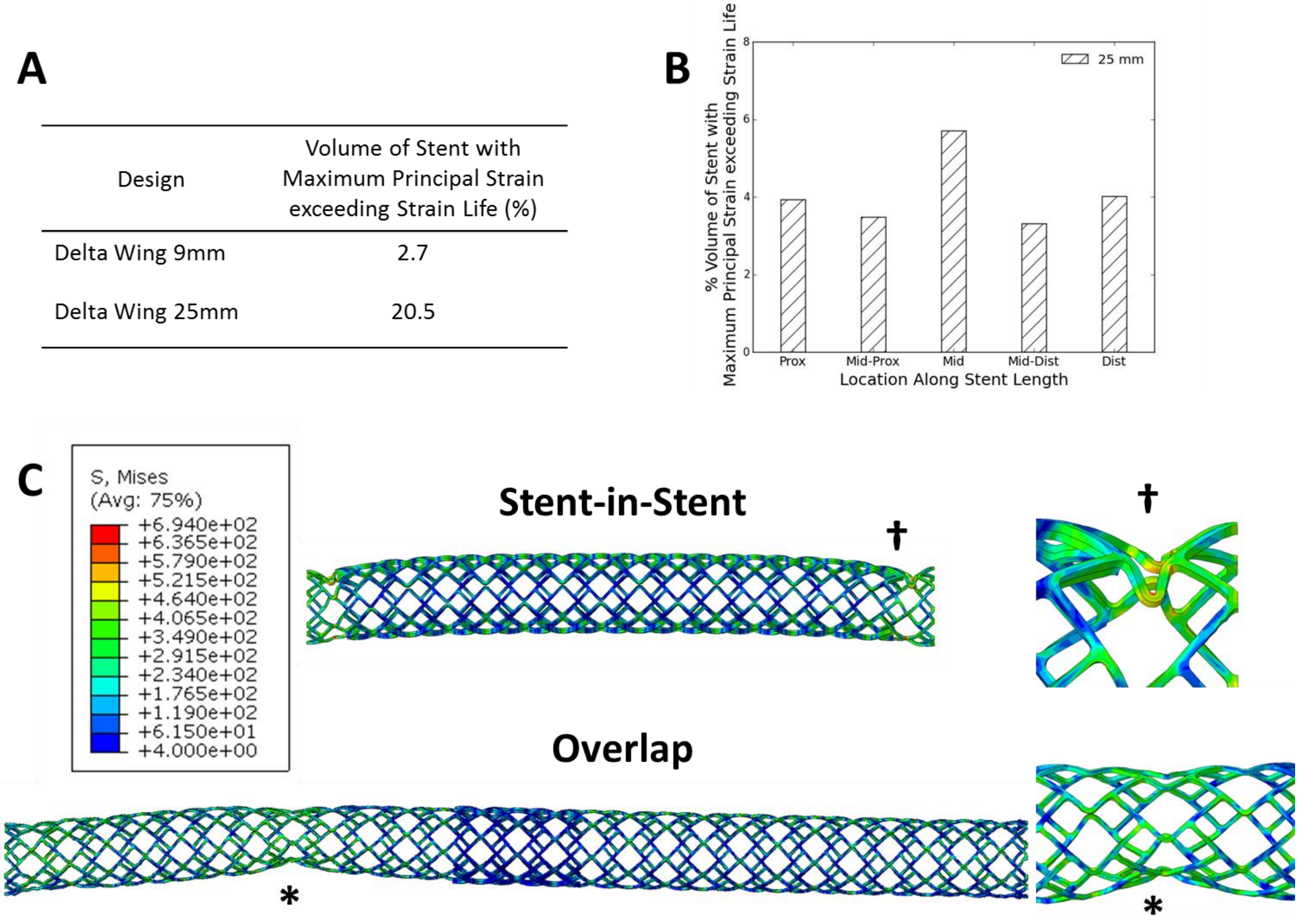

Design	Volume of Stent with Maximum Principal Strain exceeding Strain Life (%)
Delta Wing 9mm	2.7
Delta Wing 25mm	20.5

Figure 5 Predicted Stent Stresses and Strains as a Function of Stent Length – In single stents, strain is concentrated in the mid stent and this effect is enhanced in long stents (A, B). Overlap and stent-in-stent implantation results in the development of stress concentrations adjacent to the overlap site (C), with buckling type behavior that is enhanced adjacent to the stiffened overlapped regions.

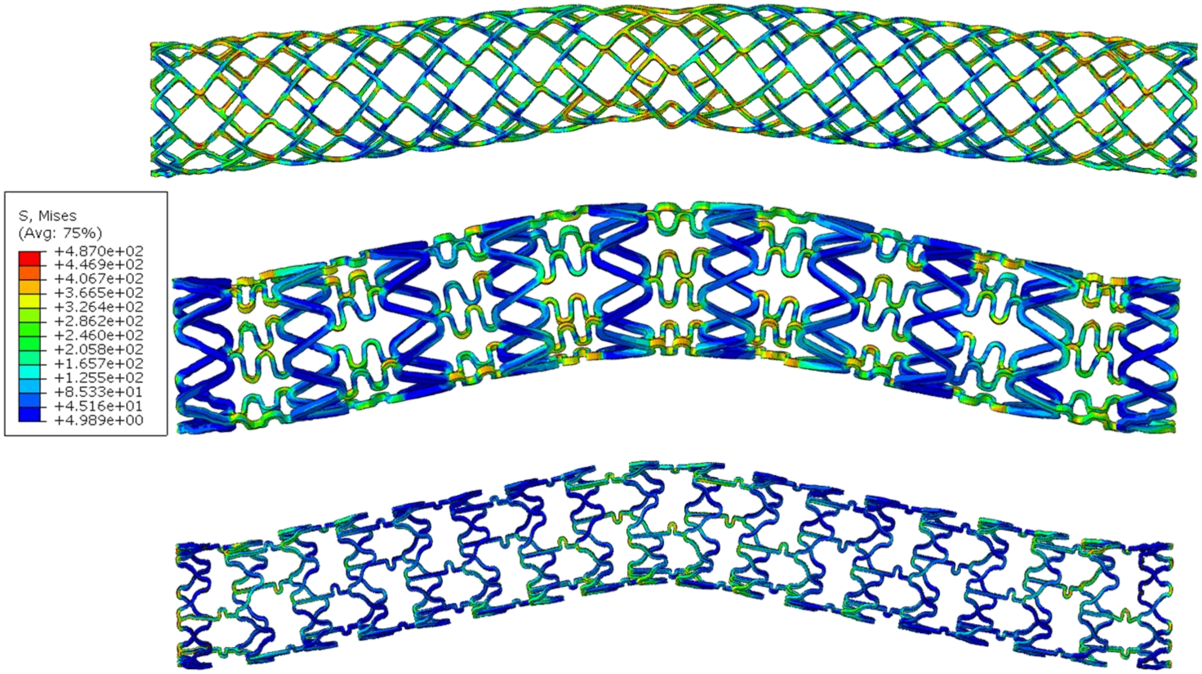

Figure 6 Deformation Behavior Transcends Stent Design – The mid-stent segment in single stents represents the location of highest von Mises stress and predicted location of highest deformation in delta wing (top), corrugated ring (center) and multilink (bottom) designs.

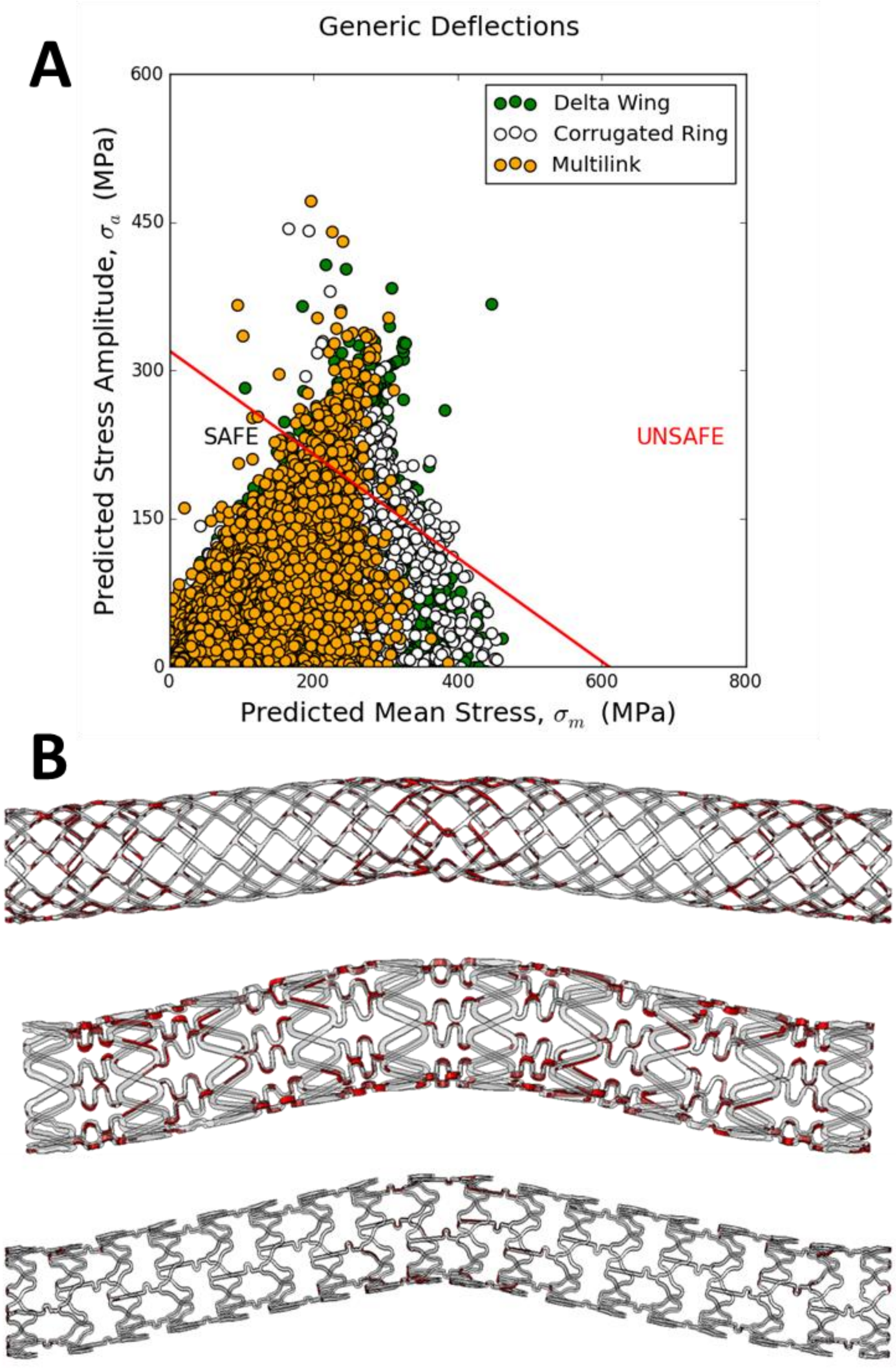

Figure 7 A) Goodman analysis for three stent designs subjected to generic multimodal deformations in terms of predicted maximum principal stress: alternating component versus mean component, B) Predicted unsafe areas (highlighted in red) according to the Goodman Analysis of three stent designs; top - delta wing, middle - corrugated ring and lower - multilink.

Supplementary Methods (for inclusion in online publication)

Finite Element Analysis

3D stent geometries were created in the commercially available finite element software, Abaqus (Dassault Systems, MA, USA, v6.10-EF). The geometries for each stent design are constructed in straight deployed states to which boundary conditions are applied. The as-deployed orientation was selected to avoid effects of rotational asymmetry inherent in the complex features of the stent unit cell. Solid, homogeneous, elastoplastic material models with strain hardening for biomedical grade 316L stainless steel were applied with: isotropic elasticity with Young's Modulus 200 GPa , density 7900 kg/m^3, and Poisson's ratio 0.3 [46]. Plastic strain values took into account dimension-dependent mechanical behavior, including linear kinematic plastic hardening with yield at 400 MPa [46]. Eight-noded, reduced integration, hexahedral elements were selected for their ability to predict global large deformation behavior. Mesh sensitivity studies were performed using the Abaqus/Explicit solver and resulted in the total number of elements of 70000, 64800, 122706 and elements per cross-section (width x thickness) of 4 x 2, 3 x 3, 4 x 3 elements for the delta wing, corrugated ring and multilink designs, respectively. Boundary conditions were applied using multipoint constraints (MPCs), created using rigid beam elements to link reference points located at the central longitudinal access with the outer faces of each end of the stent as per the approach of [47] and as illustrated in Figure 1 for the delta wing design.

Three different stent geometries were chosen to model an array of open and closed cell designs and probe the spectrum of currently available designs. In addition to the three stent geometries, finite element models of overlapped and stent-in-stent implantation geometries were performed; contact of elements within a single stent was included but contact between overlapping devices was not modelled. Increasingly long stents, in as-distributed dimensions, were also created.

Deformations were acquired from cardiac-gated CT images described above and supplemented with published strain data for stented coronary [18–21], mid LAD and ostial RCA segments [48] (Table 2). All deformations were applied in simultaneous multimodal fashion for multiple fully reversed cycles to incorporate the dynamic motions of the cardiac cycle. Specifically, nodes at the proximal and distal ends of the stent mesh had three degrees of freedom with applied deformations corresponding to axial (Z-axis) motion, rotational motion around the Y-Z plane and rotational motion around the X-Y plane respectively (Figure 1). As a representative generic artery case, values within the spectrum of those observed on a per-artery basis were selected. Deflections representative of the ostial right (oRCA) and mid-proximal (mpLAD) coronary arteries were also chosen. Differential boundary conditions were enforced, specifically in the oRCA case, by fully constraining the one MPC node, representing the ostial, and applying displacement to the other MPC node, representing the more freely mobile distal segment.

Given the highly dynamic nature of the *in vivo* environment, the dynamic predicted response of the global device in terms of stress and strain is of great interest to this work. Results are presented in terms of contour plots illustrating spatially the von Mises stress distributions and also the ranges of particular strain variables at the final loading state for each case. The temporal development of this stress state is shown in supplementary material for each of the three stent designs.

Goodman Fatigue Analysis

Following FEA of the three stent designs subjected to multimodal symmetric deformations a Goodman fatigue analysis was performed. From the final cycle of multimodal deformation, the maximum principal stresses were extracted from each stenting simulation in the maximally loaded state (cycle peak) and unloaded state (cycle trough). The mean stress, σ_m, and alternating stress, σ_a, are calculated and plotted for each of the three stent designs.

In a Goodman analysis fatigue failure is expected to occur if the stress state satisfied the following equation:

$$\frac{\sigma_a}{\sigma_N}+\frac{\sigma_m}{\sigma_{UTS}}\geq 1$$

where σ_a is the amplitude of cyclic stress ($\sigma_a = \left|\sigma_{Max\,principal}^{Max\,Load} - \sigma_{Max\,principal}^{Unload}\right|/2$), σ_m is the mean of the predicted applied stress ($\sigma_m = (\sigma_{Max\,principal}^{Max\,Load} + \sigma_{Max\,principal}^{Unload})/2$), σ_N is the fully reversed (zero mean stress) fatigue strength and σ_{UTS} is the ultimate tensile strength. The predicted stress results are plotted in comparison to a critical failure line which divides the stress space into safe and unsafe zones. The line is defined by the fatigue strength and ultimate tensile strength for 316L stainless steel: fatigue strength = 320 MPa [39] and UTS = 610 MPa [39].

Other stress-based fatigue prediction methodologies could be implemented such as the Dang Van [49] or Sines [50] or Crossland [51] criteria but the Goodman approach was adopted as it is implemented in many other published works on stent fatigue [29,32,33,36,39].

Supplementary Figures (for inclusion in online publication)

Supplementary Table I Stent Designs Associated with Strut Fracture

	Fx +	Fx -	p Value
BMS			
Minivision	1 (3.4)	36 (36.0)	<0.001
Vision	2 (6.9)	39 (39.0)	<0.001
Express 2	3 (10.3)	0 (0.0)	0.01
NIR Royal	2 (6.9)	0 (0.0)	<0.05
Omega	2 (6.9)	0 (0.0)	<0.05
Bx velocity	3 (10.3)	0 (0.0)	0.01
Driver	6 (20.7)	0 (0.0)	<0.001
Integrity	2 (6.9)	0 (0.0)	<0.05
Other	8 (27.6)	25 (25.0)	0.81
DES			
Xience	37 (6.3)	11 (1.8)	<0.001
Promus	21 (3.6)	1 (0.2)	<0.001
Taxus	35 (6.0)	475 (77.1)	<0.001
Cypher	472 (80.7)	124 (20.1)	<0.001
Endeavor	14 (2.4)	3 (0.5)	0.003
Other	6 (1.0)	2 (0.3)	0.10

Values are mean ± SE or n (%). Fx+ = Patients with adverse events and stent fracture, Fx- = Patients with adverse events not including stent fracture. BMS = bare metal stent; DES = drug eluting stent

Supplementary Table II Dynamic Curvature of Stented Coronary Arteries *in vivo*

				Radius of Curvature (cm)		
Case	Stented Vessel	Vessel Subsegment	Stents Implanted	Diastole	Systole	Change (%)
1	LAD	opLAD	1	3.72	2.94	-21.2
2	LAD	mpLAD	1	3.54	3.13	-11.5
3	LAD	pLAD thru mid mLAD	2	3.94	3.21	-18.4
4	RCA	mpRCA	1	2.82	3.39	20.3
5	LAD	pLAD	1	2.89	3.11	7.6
6	RCA	pRCA	1	2.96	3.9	31.6
7	LAD	pLAD	2	5.27	4.45	-15.6

LAD = left anterior descending, m = mid, mp = mid proximal, op = ostial-proximal, p = proximal, RCA = right coronary artery

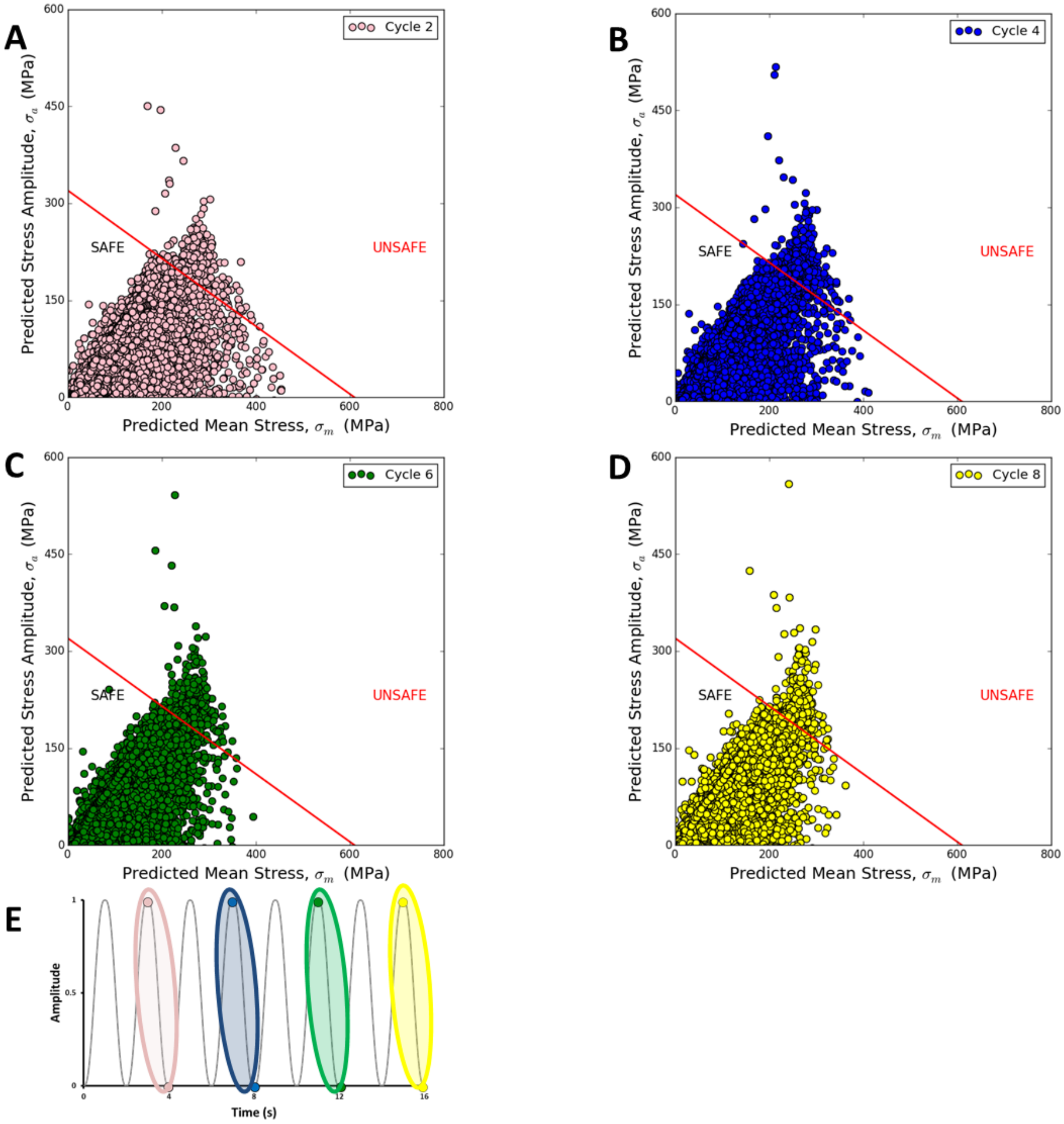

Supplementary Figure 1 Predicted Goodman analysis at 4 time points for the corrugated ring stent design. Goodman analysis for A) cycle 2, B) cycle 4, C) cycle 6, D) cycle 8, and E) amplitude of applied loading curve.

Supplementary Videos (for inclusion in online publication)

Supplementary Video 1. Dynamic Multi-Cycle Deformation of Delta-Wing Stent – The delta-wing design is able to distribute modest deformations along the length of the stent, but upon fully reversed loading experiences focal, high stress deformation and radial compression at the mid stent segment.

Supplementary Video 2. Dynamic Multi-Cycle Deformation of Corrugated-Ring Stent – The corrugated-ring design exhibits early, focal deformation in the connector elements at the mid stent, with little distribution of the load along the length of the device.

Supplementary Video 3. Dynamic Multi-Cycle Deformation of Multilink Stent – The multilink design demonstrates more uniform, distributed deformation along the length of the stent, due to its relatively lower longitudinal stiffness compared to delta-wing and corrugated-ring designs.